NJC

PAPER

View Article Online
View Journal | View Issue

Cite this: *New J. Chem.*, 2019, **43**, 18451

Molecular modeling of cytotoxic activity of a new terpenoid-like bischalcone†

Lóide O. Sallum, *[a] Vera L. Siqueira,[b] Jean M. F. Custodio,[a] Nádia M. Borges,[a] Aliny P. Lima,[bc] Davi C. Abreu,[c] Elisângela de P. S. Lacerda,[c] Rosa S. Lima,[b] Alisson M. de Oliveira,[b] Ademir J. Camargo[a] and Hamilton B. Napolitano *[ad]

Received 3rd July 2019,
Accepted 16th October 2019

DOI: 10.1039/c9nj03452h

rsc.li/njc

This study describes the synthesis and structure of (1*E*,4*E*)-1-(3-chlorophenyl)-5-(2,6,6-trimethylcyclohex-1-en-1-yl)penta-1,4-dien-3-one (BC **I**). X-ray single-crystal diffraction and Hirshfeld surface analysis describe supramolecular arrangement and topological analysis. Theoretical calculations, such as QTAIM, frontier molecular orbital, MEP and infrared spectra assignments, were performed at the B3LYP/6-311++G(d,p) level of theory. Also, this work evaluates molecular docking against DNA (PDB ID: 1BNA) and cytotoxic activity against two tumor cell lines. The BC **I** molecule has a half chair conformation of the cyclohexene ring, and the supramolecular arrangements are stabilized by C_6–$H_6\cdots O_1$ and C_7–$H_7\cdots O_1$ interactions. MEP and docking analyses indicate an electrophilic attack that is likely to occur on the carbonyl group.

Introduction

Structural modifications in organic compounds with known biological potential might increase their potential activity.[1–5] Among these important compounds, chalcones have been widely used because their pharmacophore site is similar to those found in flavones and isoflavones (potent inhibitors of DNA topoisomerase II).[6] Added to this, chalcones have a delocalized π-system composed of a carbonyl group, olefin portion and aromatic rings, which enables their interaction with biological receptors[7–12] and is responsible for some activities such as antitumor,[1,2] anti-inflammatory,[3] antiallergic[4] and antimicrobial.[5] In this sense, several chalcone derivatives have been reported to exhibit significant DNA binding interactions acting as potent anticancer agents.[13–17] Usually, these compounds are synthesized from the Claisen–Schmidt condensation of an acetophenone and a benzaldehyde, but these reactants can be altered to increase their biological activities.[18]

Another important aromatic class of compounds is β-ionones, which occur in many essential oils, such as those from roses, violets, boronias and petunias.[19,20] In food, they are present in pro-retinoid carotenoids (β-carotene) of carrots, roasted almonds, herbs and fruits.[21,22] Naturally originating from carotenoids and synthesized from citral and acetone, β-ionones are composed of a trimethylcyclohexene, an olefin portion and a carbonyl group. They have been studied not only because of their application in the fragrance industry, but also as anti-inflammatory[23,24] and anticancer[25] agents. Although the biological potential of chalcones and β-ionones is well known, their fusion into a terpenoid-like bischalcone has not been extensively studied so far. Fundik and coworkers synthesized some of these hybrid compounds by reacting α- and β-ionones with substituted benzaldehydes, furfural, and thiophene-2-carbaldehyde and evaluated their antibacterial and antifungal activity.[25] Also, Lima and coworkers[25] prepared eight new chalcones with both these structural frameworks and tested them against three cancer cell lines: SF-295, HCT-116 and OVCAR-8.

Considering the known biological properties of such hybrid compounds, BC **I** was synthesized from β-ionone and 3-chlorobenzaldehyde, and its molecular and supramolecular architectures were described using single crystal X-ray diffraction (XRD) and Hirshfeld surface (HS) analysis. In order to achieve better insights into the molecular structure, frontier molecular orbital (FMO), molecular electrostatic potential (MEP) chemical reactivity, vibrational assignment and quantum theory of atoms in molecules (QTAIM) analyses at the B3LYP/6-311++G(d,p) level of theory were undertaken. In addition, the mouse tumor lines sarcoma 180 (S-180) (ATCC® TIB-66) and Ehrlich tumor (ATCC® CCL-77) were used in biological assays, which were also investigated at the molecular level *via* docking simulations.

[a] *Grupo de Química Teórica e Estrutural, Universidade Estadual de Goiás, Anápolis, GO, Brazil. E-mail: loide.sallum@gmail.com, hbnapolitano@gmail.com; Tel: +55-(62)-3328-1192*
[b] *Faculdade do Instituto Brasil, Anápolis, GO, Brazil*
[c] *Instituto de Ciências Biológicas, Universidade Federal de Goiás, Goiânia, GO, Brazil*
[d] *Laboratório de Novos Materiais, Centro Universitário de Anápolis, Anápolis, GO, Brazil*

† CCDC 1936534. For crystallographic data in CIF or other electronic format see DOI: 10.1039/c9nj03452h

Experimental and computational procedures

Synthesis and crystallization

A bischalcone like-terpenoid was synthesized using a volumetric flask reactor of 50 mL size, to which was added 10 mL of methanol, β-ionone (1.5 mM) and 3-chlorobenzaldehyde (2.5 mM) with a high purity rate. Then, five drops of 30% aqueous potassium hydroxide solution was added into the reactional medium. The reaction mixture was shaken for 90 minutes at room temperature. At the end of the reaction time, the mixture was treated with HCl solution (10%), washed with water and then dichloromethane was added to the separation funnel to drag out the organic phase. Dichloromethane was evaporated at room temperature for 24 hours and then isopropyl alcohol was added for compound recrystallization, as shown in Scheme 1. The synthesis process was accompanied by thin-layer chromatography. Claisen-Schmidt methodology was used in the experimental protocol. Infrared spectra (IR) were recorded on a PerkinElmer Frontier in the range of 4000–700 cm^{-1} using the attenuated total reflection (ATR) technique. ATR-FTIR (cm^{-1}): 3020, 2955, 2930, 2867, 1647, 1617, 1583, 1475, 1431, 1357, 1324, 1267, 1204, 1180, 1134, 1093, 1078, 998, 906, 871, 784, 715, 703.

Crystallographic characterization

Single crystal XRD data collection was performed on a Bruker APEX II CCD diffractometer using graphite monochromated MoKα radiation (0.71073 Å) at 296 K. The structure was solved using Olex2,[26] with the ShelXS[27] structure solution program using direct methods and refined with the ShelXL[28] refinement package using least squares minimization. Olex2 was also used to prepare the crystallographic information file (CIF). The non-hydrogen atoms were refined anisotropically. The hydrogen bonded to carbon was placed geometrically and refined using a riding model with a distance of methyl C–H = 0.96 Å, methylene C–H = 0.97 Å and aromatic C–H = 0.93 Å. In the case of hydrogens, their U_{iso} was set to 1.2 U_{eq} of the bonded carbon, except for the methyl group, whose $U_{iso}(H) = 1.5\ U_{eq}$ of the corresponding carbon. The programs Ortep[29] and Mercury (version 3.10)[30] were used to prepare the artwork representations for publication. The intermolecular interactions were checked by Platon software.[31] The BC **I** molecule was deposited in the Cambridge Structural Database under code 1936534.†

The HS[32] is a spatial map used to visualize the surface of molecules that compares the electron density of a molecule with that of the entire crystal and measures the distribution of close contact interactions. We can explain the intermolecular interaction by using this tool, which is helpful to study the crystal packing behavior. In a HS, d_e is the distance from the nearest nucleus of an outside molecule to the surface, which provides the close intermolecular contacts, while d_i is the distance from inside to the surface, which provides studies of the molecule itself. The normalized contact distance (d_{norm}), which combines the normalized d_e and d_i with the van der Waals radius for each atom involved in this close contact with the surface, is used to analyze intermolecular interactions.[33] Fingerprint[34] plots provide quantitative information on the type of intermolecular contacts as well as their frequency. The software Crystal Explorer 3.1[35] was used to generate HS intermolecular interactions and calculated 2D fingerprint plots.

Theoretical calculations

Electronic structure calculations were carried out using the Gaussian 09[36] program package for BC **I**. The full geometry optimization was carried out using density functional theory (DFT) with the exchange–correlation functional B3LYP[37] and the basis set 6-311++G(d,p).[38,39] This functional is commonly used in quantum chemistry for geometry optimization. The studied electronic properties included frontier molecular orbital energies: highest occupied molecular orbitals (HOMOs) and lowest unoccupied molecular orbitals (LUMOs) and MEP. The QTAIM analysis was performed using the initial geometry generated from X-ray refinement data and assignments of infrared frequencies were also performed.

Molecular docking

Molecular docking studies were carried out using the AutoDock-Vina software.[40] Receptor and ligand were prepared using the dock prep tool of AutoDock tools implemented in the Chimera software.[41] The receptor X-ray crystallographic structure was retrieved from the Protein Data Bank (PDB)[42] and in its preparation the solvent and ligand were deleted, any hydrogens were added and the energy was minimized by the minimized structure of Chimera. The ligand assigned charge was managed with the general Amber ff12SB.[43] The receptor search volume option was enclosed in a box centered at the geometric point (13.00, 17.97, and 13.00 Å) within the grid size (43.94 × 53.77 × 47.11 Å). Chains of non-standard residues and all non-standard residues have been set to false. All other parameters were kept as the default setting.

Cell culture and cytotoxicity assay using MTT

The murine sarcoma-180 tumor cells (S180) (ATCC®# TIB-66), and Ehrlich-ascites tumor (ATCC® CCL-77™) and non-tumor cells (Vero) (ATCC® CCL-81™) were cultured in suspension in

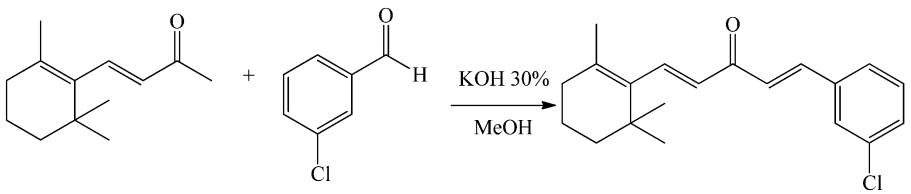

Scheme 1 Chemical scheme of the synthesized BC **I**.

RPMI 1640 and DMEM media (Sigma Chemical Co., MO), respectively, supplemented with 10% fetal calf serum, 100 μg mL^{-1} penicillin, and 100 μg mL^{-1} streptomycin. The cultures were incubated in a humidified incubator (Thermo Scientific) at 37 °C with 5% CO_2.

The cytotoxic effect of BC **I** was evaluated using MTT assay with S180, Ehrlich-ascites tumor cells and Vero non-tumor cells as described previously by Mosman, 1983.[44] Briefly, 1.0×10^5 S180 cells and 2.0×10^4 Vero cells were plated in 96-well tissue culture plates and treated with different concentrations of BC **I** and cisplatin (0.2–200 μM) for 48 h. After treatment, 10 μL of MTT (1 mg mL^{-1}) was added to each well, and the plates were incubated at 37 °C for an additional 3 h. The purple formation crystals were dissolved in 50 μL of SDS, and the absorbance was determined at 545 nm using a Stat Fax 2100 microplate reader. The cell viability was calculated and the IC_{50} was obtained from dose–response curves using GraphPad Prism 4.02 for Windows. The selectivity of BC **I** to tumor cells was assessed in terms of the selectivity index.

Cell cycle analysis and detection of apoptosis by flow cytometry

The S180 cells were treated with BC **I** (20 μM) for 24 h and 48 h. Briefly, 3.0×10^5 cells were harvested by centrifugation, washed with phosphate-buffered saline (PBS), fixed with 70% (v/v) cold ethanol and stored overnight at −20 °C. The fixed cells were washed with PBS and incubated with propidium iodide (PI; Sigma-Aldrich) containing 0.05% RNase. The samples were incubated at 4 °C in the dark and analyzed by flow cytometry (FACSCalibur, BD Biosciences). The percentage of cells in the G0/G1, S, G2/M and sub-G1 phases was analyzed using ModFit software.

The cell death of S180 tumor cells was examined using the Annexin V-FITC apoptosis detection kit. S180 cells were treated with BC **I** (20 μM) for 48 h. Briefly, 3.0×10^5 cells were harvested and washed with PBS. The cells were re-suspended in 400 μL of binding buffer. Next, 5 μL of Annexin V-FITC and 1 μL of PI were added. Flow cytometric analysis was performed immediately after supravital staining. Data acquisition and analysis were performed on a flow cytometer (FACSCalibur, BD Biosciences) using Cell Quest software. The criteria for positivity in cells in early stages of apoptosis were Annexin V-positive and PI-negative and criteria for cells in the late stages of apoptosis were both Annexin V-positive and PI-positive. Cells positive for Annexin V were stained fluorescent green and those positive for PI were stained fluorescent red.

Results and discussion

Solid state characterization

The asymmetric unit of BC **I** is shown in the Ortep diagram in Fig. 1. The stereochemistry of C7═C8 and C10═C11 is (*E*)-configuration. This molecule has a cyclohexene ring in the half chair conformation with C13 deviated by 0.205 Å from the mean plane defined by C12–C17–C16–C15–C14. This conformation also reveals the equatorial position on C11 and C13.

In the C15-flap half-chair conformation, the dihedral angles C17–C12–C13–C14 and C16–C17–C12–C13 are 11.2° and −0.3°, respectively. The molecular conformation from the β-ionone mean plane calculated through cyclohexene and core carbonyl atoms forms an angle of 49.59° observed in terpenoid-like chalcones, as shown in Fig. 2. This molecular conformation is a common structural framework present in many anticancer terpenoid-like chalcones.[45,46] The C10–C11–C12–C13 and C10–C11–C12–C17 dihedral angles are 134.0° and −47.7°. The C2–C1–C7–C8 and C6–C1–C7–C8 dihedral angles are 3.7° and −178.4°, respectively, which indicates coplanarity in this region.

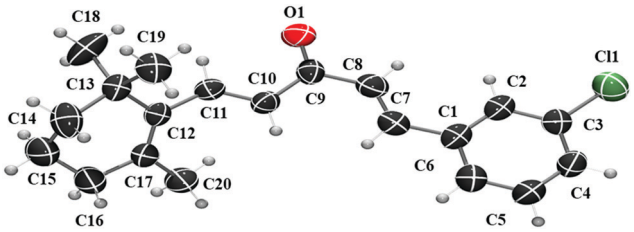

Fig. 1 Ortep diagram of ellipsoids at 50% probability level with the atomic numbering scheme for BC **I**. Hydrogen atoms are in arbitrary radii.

XRD data are shown in Table 1. BC **I** crystallized into the $P2_1/c$ space group with unit cell parameters: a = 11.4168(13) Å, b = 14.2639(18) Å, c = 11.1744(14) Å and β = 106.469(3)°. The selected bond lengths and angles and conformationally important dihedral angles are listed in Table 2. Table 2 shows theoretical and experimental geometric parameters in good agreement with one another. The major difference of about 4.59% is in contraction strengthening of the C7–C8 (1.285 Å) experimental bond, with a C7–C8 (1.344 Å) theoretical length. The theoretical calculation model suggests geometric parameters very close to experimental ones, regardless of supramolecular arrangements.

BC **I** crystal packing is stabilized by bifurcated hydrogen bonds through C_6–$H_6\cdots O_1$ and C_7–$H_7\cdots O_1$ in an $R_2^1(6)$[33] ring motif, involving a carbonyl group along the *c* axis (Fig. 3), wherein C–H groups are hydrogen bonding donors pertained to the α,β-unsaturated ketone and aromatic ring, respectively. Also, this

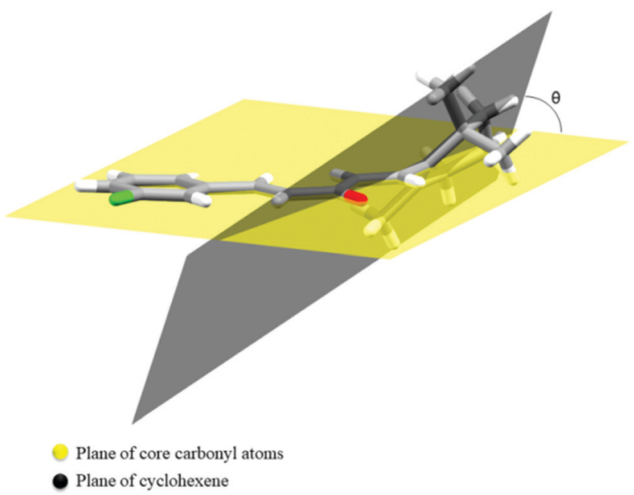

Fig. 2 Representation of angles formed by planes of core carbonyl atoms and cyclohexene for BC **I**. θ = 49.59°.

Table 1 Crystal data and structure refinement for BC **I**

Chemical formula	$C_{20}H_{23}O_1Cl_1$
MW	314.83 g mol^{-1}
Crystal system, space group	Monoclinic, $P2_1/c$
Temperature	296(2) K
a, b, c	11.4168(13) Å, 14.2639(18) Å, 11,1744(14) Å
α, β, γ	90°, 106.469 (3)°, 90°
V	1745.1(4) Å^3
Z	4
Radiation type	Mo Kα
μ (mm^{-1})	0.219
$R[F^2 > 2\sigma(F^2)]$	0.0823
w$R(F^2)$	0.2431
S	1.030
No. of reflections	3603
No. of parameters	213
H-Atom treatment	H atoms treated by a mixture of independent and constrained refinement

crystal packing is stabilized by two intermolecular hydrogen bonding C_6–$H_6\cdots O_1$ and C_7–$H_7\cdots O_1$ interactions, which caused two molecules to bind in a unit cell (Table 3).

The d_{norm} HS (ranging from −0.511 to 1.470 Å) is visualized in Fig. 4. This HS analysis is helpful in the identification of the most dominant intermolecular interactions among neighboring packs.[32] These interactions observed on d_e and d_i surfaces of BC **I** appear as two identical red spots. The red spot represents the H···O (4.1%) and O···H (4.7%) interactions.

Fig. 5 displays 2D fingerprint plots of BC **I**, where most of the contact is due to H···H contacts, which adds up to 55.3% of the HS of BC **I** (Fig. 5a) because it is an organic compound. The contributions of O···H/H···O contacts, characterized by the spikes at the bottom of the fingerprint plot, represent 8.9%, of the HS in BC **I** (Fig. 5b). As for C···H/H···C and Cl···H/H···Cl contacts of BC **I**, 20.8% and 14.2% of the HS are observed (Fig. 5c and d); however, the QTAIM analysis did not find these interactions.

Molecular modeling analysis

The root mean square (RMS) value of the compared calculated and experimental geometries obtained by structural overlapping was 0.0247, as shown in Fig. 6. The overlay shows a good agreement of geometric parameters. The cyclohexene ring exhibits dihedral angles of C14–C15–C16–C17 with the value of −45.9° (Table 2).

The FMO obtained from Kohn–Sham analysis of BC **I** was carried out at the B3LYP/6-311++G(d,p) level of theory (Fig. 7).

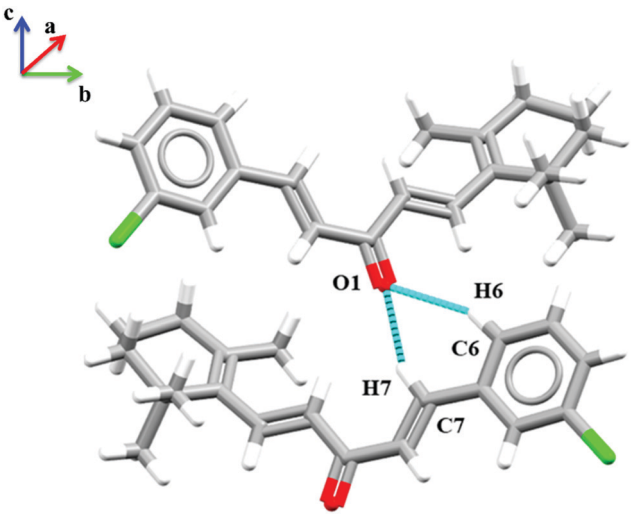

Fig. 3 Molecular arrangement of BC **I** depicting hydrogen bonds C_6–$H_6\cdots O_1$ and C_7–$H_7\cdots O_1$.

Table 3 Hydrogen-bond geometry (Å, °) for BC **I**

	D–H···A	D–H	H···A	D···A	D–H···A	Symmetry code
BC **I**	C6–H6···O1	1.04	2.59	3.563	156.00	x, 1.5 − y, −1/2 + z
	C7–H7···O1	1.04	2.37	3.354	158.00	x, 1.5 − y, −1/2 + z

The HOMO and LUMO energies are good approximations for ionization and electron affinity energies, respectively.[47] The HOMO orbital is localized on the β-ionone. The β-ionone appears to have π bonding, which is characteristic of the nucleophilic region. The HOMO energy is negative (−147.05 kcal mol^{-1}) and appears as a π bonding orbital. The LUMO orbital is a π antibonding orbital localized on the C═O bond of the carbonyl group. The LUMO energy is negative (−59.56 kcal mol^{-1}). These results show that BC **I** is an electrophilic species. This orbital analysis gives information about interactions in both occupied and unoccupied orbital spaces that could enhance the analysis of intermolecular interactions.

MEP is an important physicochemical tool that gives information about molecular interactions and is very useful to predict the reactive sites to be attacked in a chemical reaction. The electrostatic potential can be calculated through eqn (1), as follows:

$$V(\mathbf{r}) = \sum_{\alpha} \frac{Z_\alpha}{|\mathbf{r} - R_\alpha|} - \int \frac{\rho(\mathbf{r}')}{|\mathbf{r} - \mathbf{r}'|} d\mathbf{r}' \quad (1)$$

Table 2 Relevant experimental and theoretical geometric parameters for BC **I**. Bond distance (Å), angles (°) and dihedral angles (°). The calculation was carried out at the B3LYP/6-311++G(d,p) level of theory, in the gas phase

	Experimental	Theoretical		Experimental	Theoretical
C7–C8	1.285(6)	1.3445	C7–C8–C9–O1	180.0(4)	177.32
C10–C11	1.332(5)	1.3445	C6–C1–C7–C8	−178.4(4)	−179.75
C12–C17	1.341(5)	1.3547	C10–C11–C12–C17	−47.7(6)	−48.09
C17–C12–C11	123.3(3)	123.23	C12–C13–C14–C15	−41.6(5)	−46.63
C17–C12–C13	122.8(3)	122.82	C13–C14–C15–C16	60.0(6)	60.23
C2–C1–C7	123.2(4)	122.78	C14–C15–C16–C17	−45.9(6)	−42.89
C8–C7–C1	125.7(4)	127.02	C15–C16–C17–C12	17.3(6)	15.18

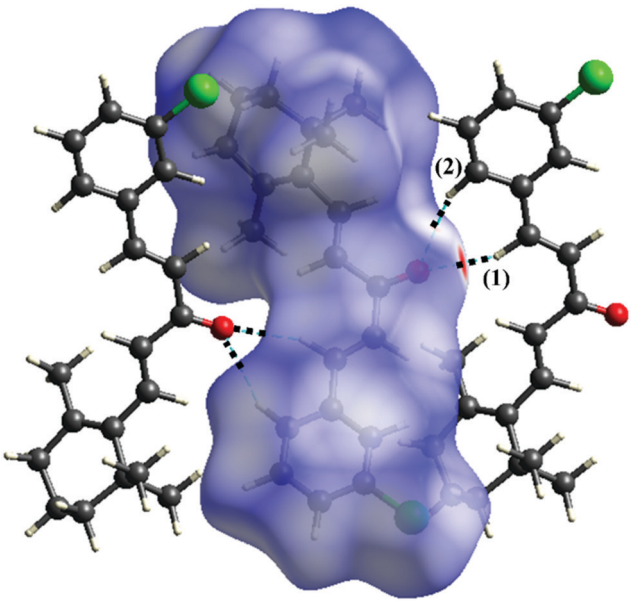

Fig. 4 Hirshfeld surfaces plotted for the BC **I** d_{norm} surface. Dotted lines are used to represent hydrogen bonds.

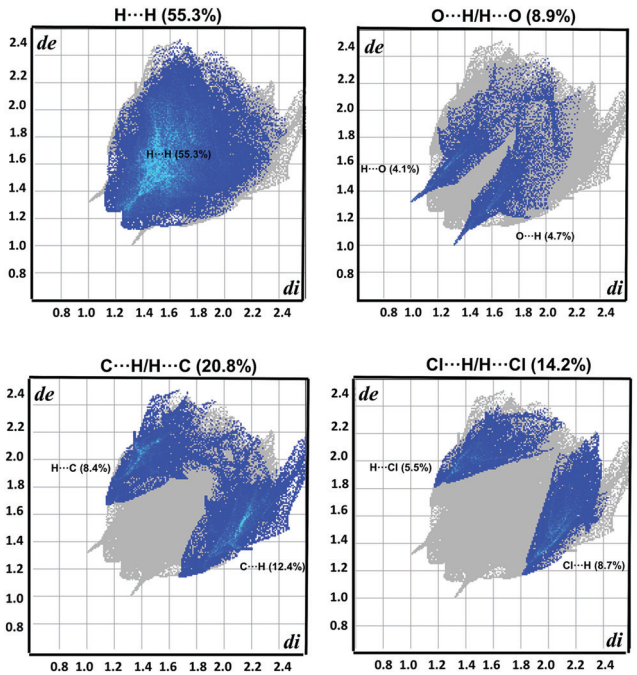

Fig. 5 Fingerprint plots for BC **I** quantifying the different types of contacts (a) H···H, (b) O···H, (c) C···H and (d) Cl···H. The full fingerprint is shown in gray. The internal distance (d_i) from a given point on the Hirshfeld surface and the closest external contact is (d_e).

where $V(\mathbf{r})$ is the potential energy with a positive unit charge at $\mathbf{r}$; Z_α is the nuclear charge α located at R_α, and $\rho(\mathbf{r}')$ is the electron density at point $\mathbf{r}'$.

To understand the MEP for BC **I**, we used the tridimensional MEP representation (Fig. 8), in which the most negative region (red) is localized on the oxygen atom of the carbonyl group,

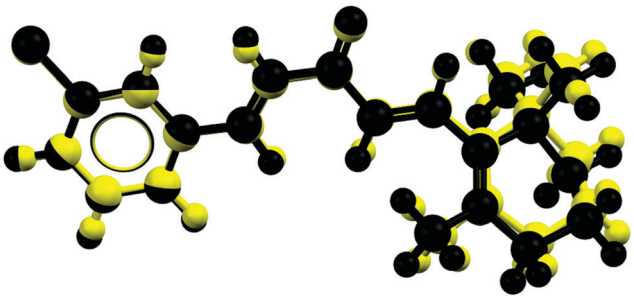

Fig. 6 Overlapping of B3LYP/6-311++G(d,p) level of theory (black) and X-ray (yellow) structures of BC **I**.

with a value of about −34.19 kcal mol^{-1}. On the other hand, the positive region (blue) is around the hydrogen atom of the α,β-unsaturated ketone, with an isovalue potential energy of about 21.65 kcal mol^{-1}. In this region, the chlorine atom at the meta position with the aromatic ring is responsible for the electron withdrawing effect. From these results, we can conclude that the electrophilic attack is likely to occur on the carbonyl group. The IR absorption bands are provided in Table 4, and the experimental and calculated FTIR spectra are shown in Fig. 9. Huang and Xing[48] scaled by 0.961 the values of DFT vibrational frequencies for the results obtained at the B3LYP/6-311++G(d,p) level of theory. In chalcones, we must consider the resonance effects of α,β-unsaturated ketones, which result in a lowering of the frequency absorptions for carbonyl groups and alkenes. The good correlation suggests that BC **I** in crystalline arrangement is very close to the computed data obtained in the gas phase.

The QTAIM analysis was carried out within the quantum chemical calculations required using Gaussian 09. This is a powerful tool to analyze the inter-atomic interactions based on electron density distribution.[49] Nevertheless, the QTAIM affects the supramolecular arrangement of molecules in the crystalline state. The Multiwfn program[50] was used within the QTAIM approach. These interactions can be described and visualized with the help of molecular graphs, and they show a crucial bond path linking the proton-acceptor atoms, as shown in Fig. 10 and Table 5.

BC **I** is formed by two hydrogen bonds (C_6–$H_6\cdots O_1$ and C_7–$H_7\cdots O_1$). The bond critical point (BCP) describes the stationary point between these hydrogen donor atoms and the acceptor atoms as a confirmation of the existence of hydrogen bonding interaction; for the electron density at the BCP of the proton-acceptor, $\rho(\mathbf{r})$, a value of 0.022 a.u. was calculated for C_6–$H_6\cdots O_1$ and 0.017 a.u. for C_7–$H_7\cdots O_1$ (in the range of 0.002–0.040 a.u. typical of hydrogen bonds); the second Hessian eigenvalue λ_2 is negative (so sign λ_2) and identifies the bonding interaction; the positive Laplacian, between 0.028 and 0.032 for C_6–$H_6\cdots O_1$ and C_7–$H_7\cdots O_1$, respectively, is observed for noncovalent hydrogen bond interactions. The total energy density value $E(\mathbf{r})$ is small and negative for C_6–$H_6\cdots O_1$, and C_7–$H_7\cdots O_1$.

The hydrogen bond energy (E_{HB}) is the energy obtained from the interaction energy. According to Espinosa–Molins–Lecomte,[51] the electron density at the BCP permits the

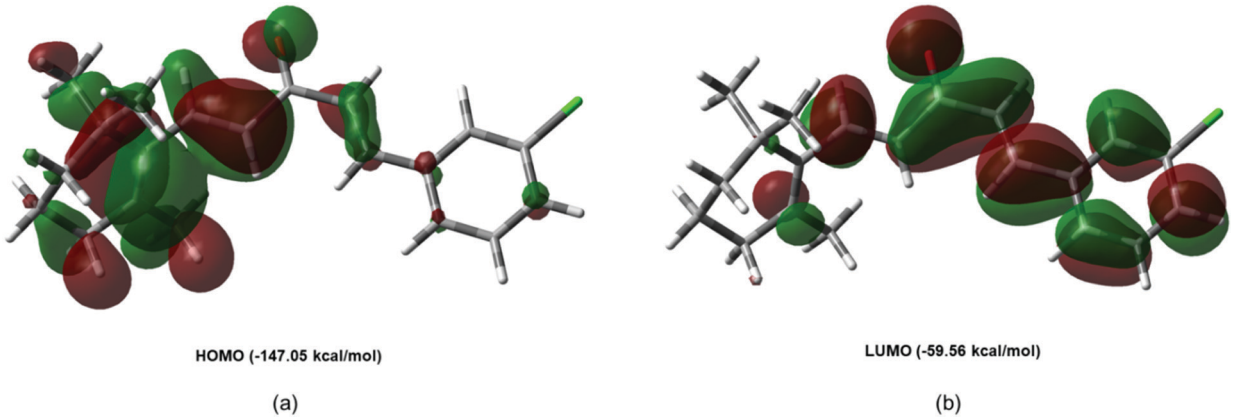

Fig. 7 Frontier molecular orbitals for BC **I** derived from Kohn–Sham analysis at the B3LYP/6-311++G(d,p) level of theory with the isovalue of 0.02 atomic units.

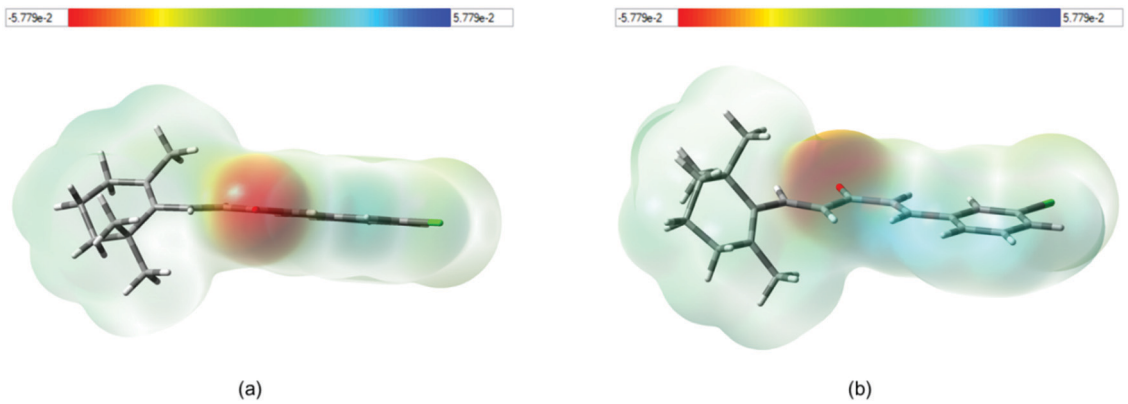

Fig. 8 Molecular electrostatic potential surface mapped for BC **I**. (a) The red-coloured carbonyl region is rich in electrons, and (b) the blue-coloured region is electron-depleted. The density isovalue of 4.0×10^{-4} electrons per $Bohr^3$ was used to generate the molecular electrostatic potential surfaces.

correlation of E_{HB} to the potential energy of the electrons $V(\mathbf{r}_{bcp})$, as shown in eqn (2):

$$E_{HB} = \frac{1}{2}V(\mathbf{r}_{bcp}) \quad (2)$$

High values of E_{HB} and the modulus of $V(\mathbf{r}_{bcp})$ are indicative of covalence if $|V(\mathbf{r}_{bcp})| > 2|G(\mathbf{r}_{bcp})|$ and $\nabla^2\rho(\mathbf{r}) < 0$. According to Rozas,[52] these interactions have a hydrogen bond energy E_{HB} below 12 kcal mol^{-1}, which is classified as weak. The α,β-unsaturated group is stabilized by hydrogen bonds of C–H···O linking them with oxygen at the carbonyl group. In addition, the hydrophobic interaction contributes to this structural stability.

DNA docking analysis

DNA represents a traditional target for a wide range of anti-cancer drugs, especially in regions of DNA involved in vital processes.[53,54] Drug–DNA interaction could change the DNA structure as well as the cell metabolism and even terminate cell growth. Along these lines, the development of new drugs that have improved toxicity and pharmacokinetic profiles is critical. In order to explore the interaction mechanisms and progress with the design of a specific DNA target drug, the determination of binding

Table 4 Theoretical and experimental vibrational assignments for BC **I**. The calculation was carried out at the B3LYP/6-311++G(d,p) level of theory, in the gas phase

Vibrational mode	Exp. freq.[a]	Scaled freq.[a,b]
$\nu_{sym/asym}(C–H)_{Ar}{}^{c}{}_{,Alk}{}^{d}$	3020–3000	3010–3000
$\nu_{sym/asym}(CH_3)$ and $\nu_{sym/asym}(CH_2)$	2955–2867	2974–2857
$\nu(C{=}O)$	1647	1636
$\nu(C{=}C)_{Ar}{}^{c}$	1617; 1475	1615; 1566; 1402
$\nu(C{=}C)_{Hex}{}^{e}$	1583	1566
$\nu(C–C)_{Hex}{}^{e}$	1324	1321
$\delta(CH_3)$ in plane	1431	1441
$\delta(C–H)_{Alk}{}^{d}$ in plane	1267	1285
$\delta(C–H)_{Hex}{}^{e}$ out of plane	1180	1168
$\delta(C–H)_{Hex}{}^{e}$ and $\delta(C–H)_{Alk}{}^{d}$ in plane	1134	1114
$\nu(C–C)_{Hex}{}^{e}{}_{/Alk}{}^{d}$ and $\delta(C–H)_{Hex}{}^{e}$ in plane	1093	1089; 1109
$\delta(C–H)_{Ar}{}^{c}$ in plane	1078; 1204	1051; 1144
$\delta(C–H)_{Alk}{}^{d}$ out of plane	998;	966; 1001
$\delta(CH_3)$ out of plane	906; 1357	1345
$\delta(C–H)_{Ar}{}^{c}$ and $\delta(C–H)_{Alk}{}^{d}$ out of plane	871	880
$\delta(C–H)_{Ar}{}^{c}$ out of plane	784	766
$\delta(C–CO)$ and $\delta(C–H)_{Hex}{}^{e}$ in plane	715	713
$\nu(C–Cl)$	703	705

ν = stretching; δ = bending; sym = symmetric; asym = asymmetric; [a] cm^{-1}. [b] Scale factor 0.961. [c] Ar = aromatic ring. [d] Alk = alkene. [e] Hex = cyclohexene ring.

mode is crucial. Because of the problems and monetary costs of experimental strategies for determining the crystallographic structure of the complex, *in silico* methods are sought, to predict binding modes.[54]

The interaction of BC **I** with DNA (PDB ID: 1BNA) was investigated by molecular docking,[55] and the lowest energy according to the AutoDock scoring function was selected. The study revealed a good binding affinity with DNA and the highest affinity of −6.9 kcal mol^{-1} docking energy. Generally, all poses have shown high capability to bind DNA in a groove binding mode. Fig. 11 shows that the bischalcone was completely enfolded in the minor groove of the targeted DNA and stabilized by van der Waals interaction and hydrophobic contacts in the GC-rich region. In particular, minor groove binders are an important series of derivatives in anticancer treatment.[54] In this model, the compound BC **I** formed two hydrogen bonds between the oxygen atom of the carbonyl group and hydrogen of two guanines, which are DG16 and DG10, with the bond length of 2.42 Å and 1.88 Å, respectively, as shown in Fig. 12. In this manner, an accessible acceptor atom in the compound, which is involved in hydrogen bonding with hydrogen of guanine, assumes an essential role in the DNA binding studies of bischalcone. Consequently, a good correlation between previous theoretical outcomes and molecular docking provides valuable information on the interaction of BC **I** with DNA, since there is no co-crystallization with DNA information.

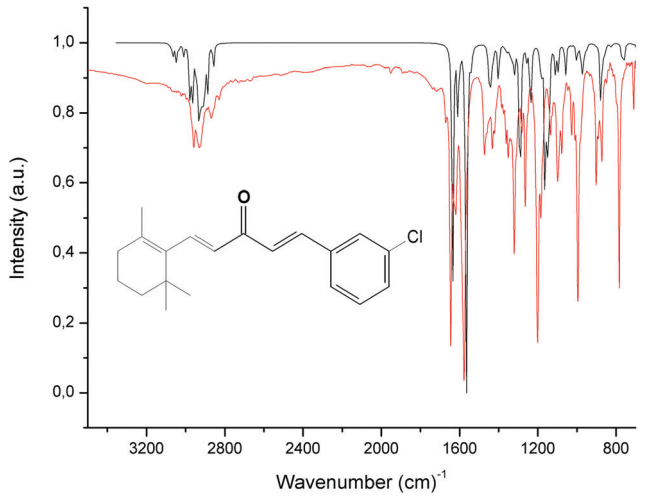

Fig. 9 Experimental (red) and theoretical (black) overlapped FT-IR spectra of BC **I**.

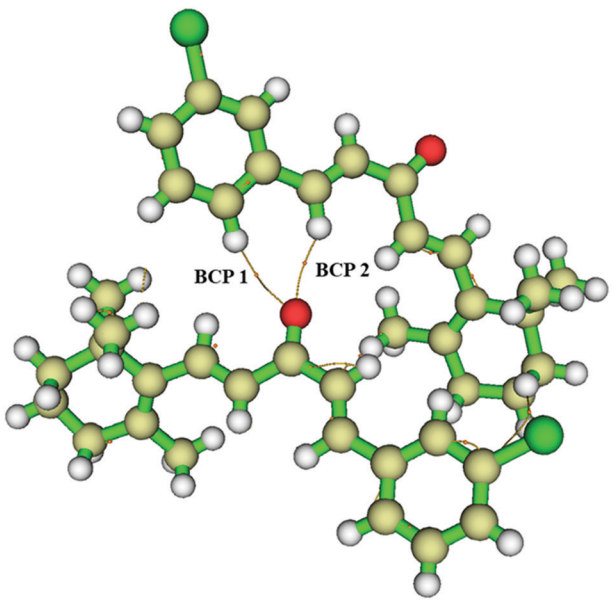

Fig. 10 Molecular graphs showing the BCP yellow points.

Cytotoxic activity

The cytotoxic activity of BC **I** for the tumor cell line S180, Ehrlich-ascites and non-tumor Vero cells was assayed by observing cell viability after 48 h of exposure. Fig. 13 shows the dose–response curves for S180 (a), Ehrlich-ascites (b) and Vero cells (c) analysed by MTT assay.

As shown in Table 6, BC **I** inhibited the viability of the S180 and Ehrlich-ascites tumor cell lines, with IC_{50} values of 19.83 μM and 38.35 μM, respectively. The results in Table 6 and the dose–response curves in Fig. 13a and b show that BC **I** is more active against S180 cells compared with the Ehrlich-ascites cells. Under the same conditions, cisplatin showed IC_{50} values of 29.05 μM against S180 tumor cells and 62.42 μM against Ehrlich-ascites tumor cells (Table 6). In particular, BC **I** has a higher SI^a of 1.33 for S180 cells and SI^b of 0.68 for Ehrlich-ascites tumor cells compared with cisplatin, with the SI^a of 0.3 (S180) and SI^b of 0.15 (Ehrlich-ascites). These results suggest that BC **I** is generally more selective for S180 cancer cells compared with Vero non-tumor cells.

The cytotoxic activity of chalcone and chalcone derivatives can result from cycle cell arrest, induction of death cell, or a combination of these two mechanisms.[56,57] Flow cytometric analysis was performed to determine the possible cytotoxicity mechanisms of BC **I** in S180 tumor cells. As shown in the cell cycle analysis (Fig. 14), exposure of the S180 cells to BC **I** led to a significant increase in the percentage of cells in the G0/G1 and S phases, which was accompanied

Table 5 Topological parameters of BC **I** describing intermolecular interactions (electron density at BCP ($\rho(\mathbf{r})$)), Laplacian ($\nabla^2\rho(\mathbf{r})$), the potential electron energy density ($V(\mathbf{r})$), the kinetic electron energy density ($G(\mathbf{r})$), the total electron energy density ($E(\mathbf{r})$), $|V(\mathbf{r})|/|G(\mathbf{r})|$ and bond energy (E_{HB})

BCP	Interaction	$\rho(\mathbf{r})^a$	$\nabla^2\rho(\mathbf{r})^a$	$V(\mathbf{r})^a$	$G(\mathbf{r})^a$	$E(\mathbf{r})^a$	$E_{Hb}{}^b$	Kind of interaction
1	C6–H6···O1	0.02211	0.02819	−0.00932	0.00818	−0.00113	−2.9241	Weak
2	C7–H7···O1	0.01756	0.03243	−0.01175	0.00993	−0.00182	−3.6866	Weak

[a] Atomic units. [b] kcal mol^{-1}.

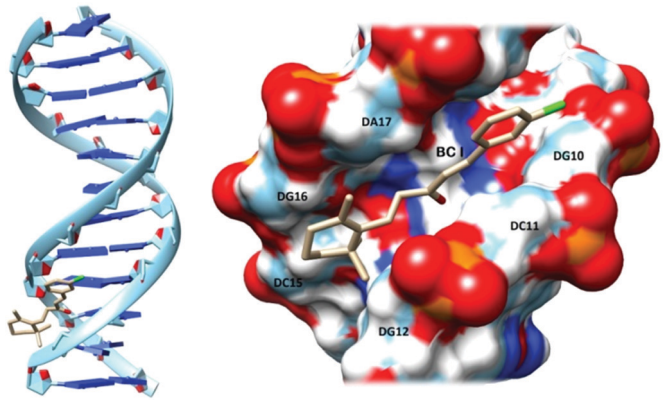

Fig. 11 Molecular docking for BC **I** with DNA (PDB ID: 1BNA).

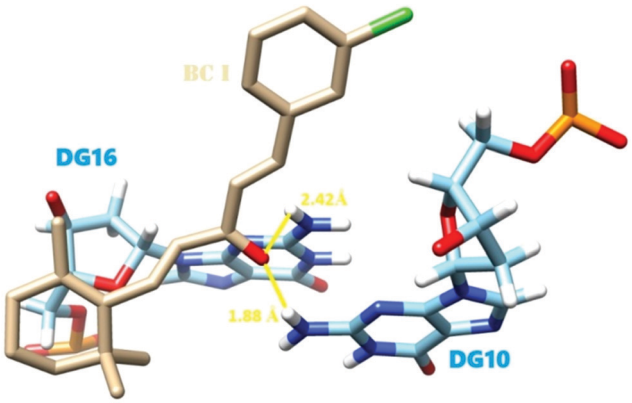

Fig. 12 Molecular docking for BC **I** showing two hydrogen-bonding interactions with DNA (PDB ID: 1BNA).

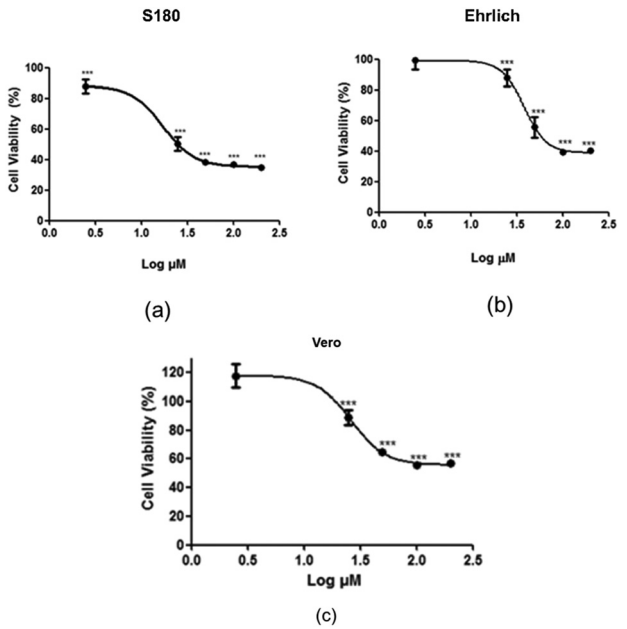

Fig. 13 Dose–response curves for (a) S180, (b) Ehrlich-ascites and (c) Vero cells analysed by MTT assay. The data are the means ± SD of three experiments. Significant differences from the untreated control are indicated by ***$p < 0.001$.

by a corresponding reduction in the percentage of cells in the G2/M phase. The fraction of cells increased from 11.28% (phase G0/G1) and 38% (phase S) in the control to 19.26% (phase G0/G1) and 63.30% (phase S) after exposure to 20 μM BC **I**. In relation to the G2/M phase, there was a decrease in the fraction of cells from 50.70% in the control to 17.43% in cells after exposure to BC **I**.

To evaluate the mechanism of S180 cell death induced by BC **I**, the FITC-Annexin V/PI assay was used. As shown in Fig. 15a and b, after exposure of the S180 cells to 20 μM BC **I** for 48 h, the cells in initial apoptosis (Annexin V+ and PI−) represented 1.88%, cells in late apoptosis (Annexin V+ and PI+) represented 12.97% and cells in necrosis (Annexin V− and PI+) represented 39.04% ($p < 0.001$) of the total cells. The distribution of cells is shown in the dot plot in Fig. 15b. The results showed that the mechanism of S180 cell death induced by BC **I** may involve a necrosis and apoptosis process. Thus, the two

Table 6 IC_{50} (μM) and selectivity indexes (SIs) of BC **I** and cisplatin in S180, Ehrlich-ascites tumor cells and Vero non-tumor cells

IC_{50} (μM)					
	S180	Ehrlich	Vero	SI[a]	SI[b]
BC **I**	19.83 ± 1.22	38.35 ± 1.39	26.43 ± 1.49	1.33	0.68
Cisplatin	29.05 ± 1.88	62.42 ± 1.85	8.75 ± 0.25	0.3	0.14

SI[a](IC_{50} Vero/IC_{50} S180). SI[b](IC_{50} Vero/IC_{50} Ehrlich).

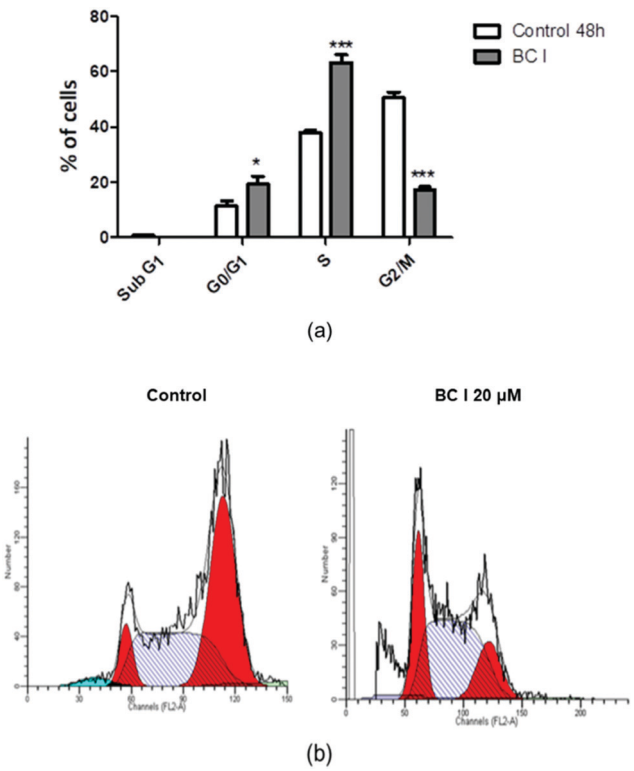

Fig. 14 Effect of BC **I** on the cell cycle distribution of S180 cells after 48 h of exposure. The data are the means ± SD of three experiments. Significant differences from the untreated control are indicated by ***$p < 0.001$.

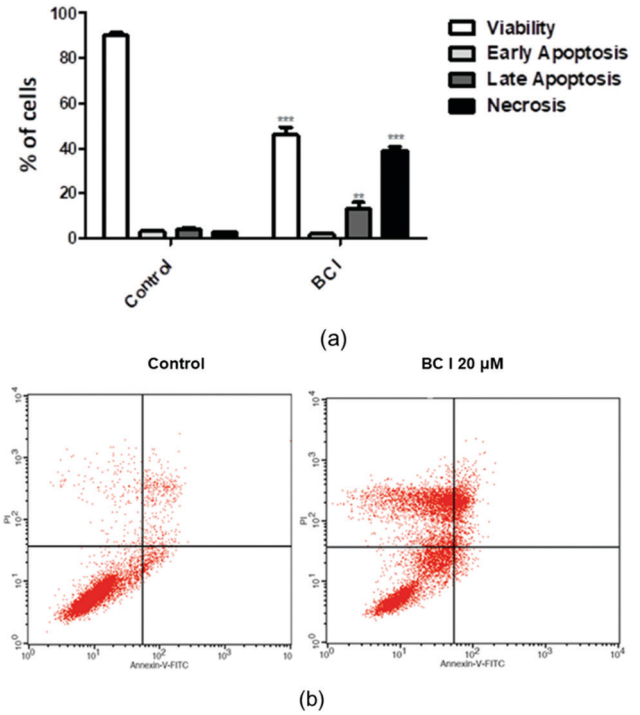

Fig. 15 Effect of BC **I** on the mechanism of S180 cell death (early and late apoptosis/necrosis) evaluated by flow cytometry after 48 h of exposure. The data are the means ± SD of three experiments. Significant differences from the untreated control are indicated by ***$p < 0.001$ and **$p < 0.01$.

types of cell death may be induced simultaneously or successively when S180 cells were exposed to BC **I**.

Conclusions

The BC **I** compound was synthesized by Claisen–Schmidt methodology using β-ionone and substituted benzaldehyde. The supramolecular arrangement was described by non-classical hydrogen C–H···O bonding, which was observed in QTAIM and topological analysis (8.9% of O···H interaction). Theoretical calculations confirmed the observed molecular conformation and electrophilic species of BC **I**. Moreover, MEP calculation indicates the susceptible electrophilic attack around the oxygen atom of the carbonyl group, which justifies the molecular docking as potent DNA (PDB ID: 1BNA) minor groove binders. Finally, the biological activity of BC **I** indicates cytotoxicity to S180 tumor cells. This cytotoxic response is associated with the inhibited cell growth through G0/G1 phase arrest and induction of necrosis and apoptosis cell death.

Conflicts of interest

The authors declare that there are no conflicts of interest.

Acknowledgements

The authors are grateful to the Coordenação de Aperfeiçoamento de Pessoal de Nível Superior (CAPES) and the Fundação de Amparo à Pesquisa do Estado de Goiás (FAPEG) for financial support. Also, the authors are grateful to the High Performance Computing Center of the Universidade Estadual de Goiás (UEG).

References

1 I. Deb Majumdar, A. Devanabanda, B. Fox, J. Schwartzman, H. Cong, J. A. Porco and H. C. Weber, *Biochem. Biophys. Res. Commun.*, 2011, **416**, 397–402.
2 J. M. F. Custodio, E. C. M. Faria, L. O. Sallum, V. S. Duarte, W. F. Vaz, G. L. B. De Aquino, P. S. Carvalho and H. B. Napolitano, *J. Braz. Chem. Soc.*, 2017, **28**, 2180–2191.
3 S. N. A. Bukhari, M. Jasamai, I. Jantan and W. Ahmad, *Mini-Rev. Org. Chem.*, 2013, **10**, 73–83.
4 T. Yamamoto, M. Yoshimura, F. Yamaguchi, T. Kouchi, R. Tsuji, M. Saito, A. Obata and M. Kikuchi, *Biosci., Biotechnol., Biochem.*, 2004, **68**, 1706–1711.
5 V. Rao, V. Rao Avupati, P. Rajendra and P. Yejella, *Chalcones*, 2014, **3**, 1713–1742.
6 H.-K. Wang, S. L. Morris-Natschke and K.-H. Lee, *Med. Res. Rev.*, 1997, **17**, 367–425.
7 E. Venkateswararao, V. K. Sharma, J. Yun, Y. Kim and S. Jung, *Bioorg. Med. Chem.*, 2014, **22**, 3386–3392.
8 Y. L. Jin, X. Y. Jin, F. Jin, D. H. Sohn and H. S. Kim, *Arch. Pharmacal Res.*, 2008, **31**, 1145–1152.
9 L. Wang, G. Chen, X. Lu, S. Wang, S. Han, Y. Li, G. Ping, X. Jiang, H. Li, J. Yang and C. Wu, *Eur. J. Med. Chem.*, 2015, **89**, 88–97.
10 L. Zhai, M. Chen, J. Blom, T. G. Theander and A. Kharazmi, *J. Antimicrob. Chemother.*, 1999, **43**, 793–803.
11 J. M. F. Custodio, L. J. Michelini, M. R. C. De Castro, W. F. Vaz, B. J. Neves, P. V. L. Cravo, F. S. Barreto, M. O. M. Filho, C. N. Perez and H. B. Napolitano, *New J. Chem.*, 2018, **42**, 3426–3434.
12 M. Go, X. Wu and X. Liu, *Curr. Med. Chem.*, 2005, **12**, 483–499.
13 Z. Chen, R. Cao, L. Yu, B. Shi, J. Sun, L. Guo, Q. Ma, W. Yi, X. Song and H. Song, *Eur. J. Med. Chem.*, 2010, **45**, 4740–4745.
14 K. R. Ethiraj, J. M. Aranjani and F. R. N. Khan, *Chem. Biol. Drug Des.*, 2013, **82**, 732–742.
15 A. Kamal, N. Shankaraiah, S. Prabhakar, C. R. Reddy, N. Markandeya, K. L. Reddy and V. Devaiah, *Bioorg. Med. Chem. Lett.*, 2008, **18**, 2434–2439.
16 H. Kumar, A. Chattopadhyay, R. Prasath, V. Devaraji, R. Joshi, P. Bhavana, P. Saini and S. K. Ghosh, *J. Phys. Chem. B*, 2014, **118**, 7257–7266.
17 N. Shankaraiah, K. P. Siraj, S. Nekkanti, V. Srinivasulu, P. Sharma, K. R. Senwar, M. Sathish, M. V. P. S. Vishnuvardhan, S. Ramakrishna, C. Jadala, N. Nagesh and A. Kamal, *Bioorg. Chem.*, 2015, **59**, 130–139.
18 J. M. F. Custodio, F. G. Santos, W. F. Vaz, C. E. P. Cunha, R. G. Silveira, M. M. Anjos, C. E. M. Campos, G. R. Oliveira, F. T. Martins, C. C. da Silva, C. Valverde, B. Baseia and H. B. Napolitano, *J. Mol. Struct.*, 2018, **1157**, 210–221.

19 C. M. Cooper, N. W. Davies and R. C. Menary, *J. Agric. Food Chem.*, 2003, **51**, 2384–2389.
20 S. Wyss, I. A. Werner, W. B. Schweizer, S. M. Ametamey and S. Milicevic Sephton, *Acta Crystallogr., Sect. C: Cryst. Struct. Commun.*, 2013, **69**, 1225–1228.
21 K. L. Simpson and C. O. Chichester, *Annu. Rev. Nutr.*, 1981, **1**, 351–374.
22 D. Belsito, D. Bickers, M. Bruze, P. Calow, H. Greim, J. M. Hanifin, A. E. Rogers, J. H. Saurat, I. G. Sipes and H. Tagami, *Food Chem. Toxicol.*, 2007, **45**, S130–S167.
23 W. Hu, M. Cai, D. Qi, X. Ying, C. Huang and C. Xing, *Pharm. Chem. J.*, 2018, **51**, 902–906.
24 C.-H. Kang, R. G. P. T. Jayasooriya, Y. H. Choi, S.-K. Moon, W.-J. Kim and G.-Y. Kim, *Toxicol. In Vitro*, 2013, **27**, 782–787.
25 X.-W. Liu, J. Yang, G.-L. Wang, Y. Gong, T.-T. Feng, X.-L. Liu, Y. Cao, Y. Zhou and W.-C. Yuan, *J. Heterocycl. Chem.*, 2018, **55**, 351–359.
26 O. V. Dolomanov, L. J. Bourhis, R. J. Gildea, J. A. K. Howard and H. Puschmann, *J. Appl. Crystallogr.*, 2009, **42**, 339–341.
27 G. M. Sheldrick, *Acta Crystallogr., Sect. C: Struct. Chem.*, 2015, **71**, 3–8.
28 G. M. Sheldrick, *Acta Crystallogr., Sect. A: Found. Crystallogr.*, 2008, **64**, 112–122.
29 L. J. Farrugia, *J. Appl. Crystallogr.*, 2012, **45**, 849–854.
30 C. F. Macrae, P. R. Edgington, P. McCabe, E. Pidcock, G. P. Shields, R. Taylor, M. Towler and J. Van De Streek, *J. Appl. Crystallogr.*, 2006, **39**, 453–457.
31 A. L. Spek, *Acta Crystallogr., Sect. D: Biol. Crystallogr.*, 2009, **65**, 148–155.
32 M. A. Spackman and D. Jayatilaka, *CrystEngComm*, 2009, **11**, 19–32.
33 J. J. McKinnon, M. A. Spackman and A. S. Mitchell, *Acta Crystallogr., Sect. B: Struct. Sci.*, 2004, **60**, 627–668.
34 M. A. Spackman and J. J. McKinnon, *CrystEngComm*, 2002, **4**, 378–392.
35 M. A. S. S. K. Wolff, D. J. Grimwood, J. J. McKinnon, M. J. Turner and D. Jayatilaka, University of Western Australia.
36 A. Goetzberger and V. U. Hoffmann, *Cytogenet. Genome Res.*, 2005, **138**, 232.
37 Y. Zhao and D. G. Truhlar, *Theor. Chem. Acc.*, 2008, **120**, 215–241.
38 A. D. McLean and G. S. Chandler, *J. Chem. Phys.*, 1980, **72**, 5639–5648.
39 R. Krishnan, J. S. Binkley, R. Seeger and J. A. Pople, *J. Chem. Phys.*, 1980, **72**, 650–654.
40 O. Trott and A. J. Olson, *J. Comput. Chem.*, 2010, **31**, 455–461.
41 E. F. Pettersen, T. D. Goddard, C. C. Huang, G. S. Couch, D. M. Greenblatt, E. C. Meng and T. E. Ferrin, *J. Comput. Chem.*, 2004, **25**, 1605–1612.
42 H. M. Berman, J. Westbrook, Z. Feng, G. Gilliland, T. N. Bhat, H. Weissig, I. N. Shindyalov and P. E. Bourne, *Nucleic Acids Res.*, 2000, **28**, 235–242.
43 J. A. Maier, C. Martinez, K. Kasavajhala, L. Wickstrom, K. E. Hauser and C. Simmerling, *J. Chem. Theory Comput.*, 2015, **11**, 3696–3713.
44 T. Mosmann, *J. Immunol. Methods*, 1983, **65**, 55–63.
45 W. B. Fernandes, L. A. Malaspina, F. T. Martins, L. M. Lião, A. J. Camargo, C. Lariucci, C. Noda-Perez and H. B. Napolitano, *J. Struct. Chem.*, 2013, **54**, 1112–1121.
46 R. S. Lima, C. N. Perez, C. C. da Silva, M. J. Santana, L. H. K. Queiroz Júnior, S. Barreto, M. O. de Moraes and F. T. Martins, *Arabian J. Chem.*, 2016, DOI: 10.1016/j.arabjc.2016.02.013.
47 T. Koopmans, *Physica*, 1934, **1**, 104–113.
48 H. Yin and X. Kong, *J. Am. Soc. Mass Spectrom.*, 2015, **26**, 1455–1461.
49 C. F. Matta and R. J. Boyd, *The Quantum Theory of Atoms in Molecules: From Solid State to DNA and Drug Design*, 2007.
50 T. Lu and F. Chen, *J. Comput. Chem.*, 2012, **33**, 580–592.
51 E. Espinosa, E. Molins and C. Lecomte, *Chem. Phys. Lett.*, 1998, **285**, 170–173.
52 I. Rozas, I. Alkorta and J. Elguero, *J. Am. Chem. Soc.*, 2000, **122**, 11154–11161.
53 R. Palchaudhuri and P. J. Hergenrother, *Curr. Opin. Biotechnol*, 2007, **18**, 497–503.
54 S. E. Sherman and S. J. Lippard, *Chem. Rev.*, 1987, **87**, 1153–1181.
55 L. O. Sallum, W. F. Vaz, N. M. Borges, C. E. M. de Campos, A. J. Bortoluzzi, C. H. J. Franco, L. M. Ramos and H. B. Napolitano, *J. Mol. Struct.*, 2019, **1192**, 274–287.
56 Z. Qi, M. Liu, Y. Liu, M. Zhang and G. Yang, *PLoS One*, 2014, **9**, e106206.
57 C. Karthikeyan, N. S. H. Narayana Moorthy, S. Ramasamy, U. Vanam, E. Manivannan, D. Karunagaran and P. Trivedi, *Recent Pat. Anti-Cancer Drug Discovery*, 2014, **10**, 97–115.

